Enhanced optical and electrical properties of Nb-doped TiO2 thin films synthesized by atomic layer deposition using the supercycle strategy

Getaneh Diress Gesesse, Olivier Debieu, Aline Jolivet, Cédric Frilay, Sylvain Duprey, Philippe Marie, Xavier Portier, Franck Lemarié, Christophe Labbé, Christian Dufour, et al.

New insights on transparent conductive Nb-doped TiO_2 thin films synthesized by the atomic layer deposition technique

Getaneh Diress Gesesse[a]*, Olivier Debieu[b], Aline Jolivet[a], Cédric Frilay[a], Sylvain Duprey[a], Philippe Marie[a], Xavier Portier[a], Franck Lemarié[a], Christophe Labbé[a], Christian Dufour[a], Clara Grygiel[a], Nithavong Cam[d], Christine Labrugere[d], Mohamad El-Roz[c], and Julien Cardin[a]*

[a] *CIMAP, ENSICAEN, UNICAEN, CEA, CNRS, 6 Boulevard Maréchal Juin, 14050 Caen Cedex 4, France*

[b] *UMR CNRS 5085 Cirimat, Institut Carnot Chimie Balard Cirimat, Université Toulouse III Paul Sabatier, 118 Route de Narbonne, 31062 Toulouse, France*

[c] *LCS, ENSICAEN, UNICAEN, CNRS, 6 Boulevard Maréchal Juin, 14050 Caen Cedex 4, France*

[d] *PLACAMAT, UAR 3626 Université de Bordeaux, CNRS, 87 Avenue du Dr Albert Schweitzer, 33608 Pessac Cedex, France*

Abstract:

Transparent Conductive Oxides (TCOs) with high optical transparency and electrical conductivity are highly attractive due to their application in various field such as optoelectronic devices, including solar cells, flat panel displays, touchscreens, light-emitting diodes, and transistors. Herein, we report new highly transparent and conductive Nb-doped TiO_2 thin films, successfully prepared by a novel low-temperature (300 °C) ALD process using titanium tetraisopropoxide, niobium(V) ethoxide, and water. The deposition was carried out by employing a supercycle approach, alternating cycles of Ti precursor followed by cycles of Nb precursor, thereby enabling precise control over the dopant concentration. We demonstrate the crucial impact of the dopant concentration played on the thickness, structure, morphology, composition, optical and electrical properties of the resulting films. The incorporation of niobium dopants led to very significant improvements on the film's characteristics. The Nb-

doped TiO_2 films exhibited an enhanced optical transmission efficiency of approximately 15%, along with a remarkable reduction in resistivity by four orders of magnitude, reaching 10^{-3} Ω.cm, compared to TiO_2 pristine film. These exceptional performances establish Nb-doped TiO_2 thin films as TCOs with wide-ranging applications in fields that require efficient current collection or injection in conjunction with optical radiation transmission.

Keywords: TCO, Nb-doped TiO_2, thin film, supercycle ALD approach, conductivity

1. Introduction

Transparent Conductive Oxides (TCOs) are a class of materials that exhibit a unique combination of high optical transparency (commonly found in metal oxides) and high electrical conductivity, which is typically not a property of oxides. These TCO materials are widely utilized as thin films in various optoelectronic devices, including solar cells, flat panel displays, touchscreens, light-emitting diodes, and transistors [1–6]. Although Sn-doped In_2O_3 (ITO) has been the industry standard TCO for a long time [7], several challenges have emerged in its widespread industrial application. The low abundance of Indium (In) [8,9] has resulted in its expensive cost [3], and concerns have been raised regarding its toxicity [10,11]. Consequently, researchers have been actively engaged in developing new TCO materials that can serve as alternative solutions to address these limitations. Some of the promising alternatives to In-based TCOs include SnO_2-based [3], ZnO-based [12–16], TiO_2-based [17–23], and other oxides. These materials are being investigated for their potential to meet the diverse requirements of TCO applications in the future, offering improved performance and sustainability.

Nb-doped anatase TiO_2 (Nb: TiO_2) is recognized as a promising candidate for TCO applications due to its high optical transparency, low refractive index, and good electrical conductivity [8,9,21,24,25]. Moreover, Nb and Ti are non-toxic, thermally and chemically stable, and more abundant in the Earth's crust compared to Indium (In) [26,27], making Nb: TiO_2 an affordable TCO material with reduced environmental impact. Nb ($5s^2 5p^3$) is considered

highly favorable as a dopant for TiO_2 because its additional electron compared to Ti ($3d^24s^2$), and its close ionic radius (0.64 Å) in respect to that of Ti (0.605 Å). This explains the limited occurrence of defects and the efficient distribution of Nb within the TiO_2 crystal lattice [27,28]. It is worth noting that although Nb is known to segregate at high temperatures, it can still be successfully incorporated into the TiO_2 lattice under suitable conditions. In the most favorable scenario, Nb doping enhances the n-type semiconductor conductivity of anatase TiO_2 by substituting pentavalent Nb for tetravalent Ti. This substitution leads to the formation of extra Ti^{3+} ions, as the Ti-3d states fall below the valence shell states of Nb. Consequently, Ti can accommodate the additional electron, resulting in the formation of Ti^{3+} ions. The increased concentration of Ti^{3+} ions, acting as shallow donors, is generally attributed to the boost in the n-type conductivity of anatase TiO_2, which leads to an increased electron population in the conduction band [29].

The Atomic Layer Deposition (ALD) technique has gained prominence in fabricating thin films of various materials for a wide range of industrial and research applications. One of the key advantages of ALD resides in its superior control over the film growth compared to the conventional deposition techniques [30–35]. ALD is a vapor phase process that involves the sequential pulsing of one or multiple precursor vapors which reacts with the substrate surface species. This process is alternat with purging steps to remove precursors' excess and the reaction by-products. The controlled pulsing and purging sequence allow the monolayers growth of the targeted material. The sequential and self-limiting nature of ALD enables precise control over the conformality, uniformity, thickness, morphology, and composition of the deposited films. Additionally, ALD operates at a low thermal budget, meaning it can achieve controlled growth at relatively low temperatures. This capability makes ALD a promising technique for achieving atomic-scale growth control while preserving the desired film properties [36–40].

So far, only a few studies have been published on the ALD of Nb: TiO_2 thin films. In 2009, Pore et al. [41] reported the first ALD fabricated Nb: TiO_2 film using titanium(IV) methoxide and

niobium(V) ethoxide as a precursor of Ti and Nb, respectively, and water as a reactant. Afterward, other researchers prepared the Nb: TiO_2 thin film using titanium(IV) chloride ($TiCl_4$) [10,42–44] and tetrakis(dimethylamido) titanium(IV) [45] as Ti precursors, and niobium(V) ethoxide [42–44] and tris(diethylamido)(tert-butylimido) niobium(V) [10,45] as Nb precursors. However, it has been reported that the combination of using $TiCl_4$ and H_2O as reactant limits the ALD process due to the corrosive nature of the precursor and the formation of HCl as a by-product. Besides, the presence of chlorine residue potentially remaining in the film can be an issue for multi-element deposition using a precursor containing cations that would easily react with chlorine to form solid chlorides [33,46]. Therefore, the choice of the precursor needs to be restrained as non-corrosive, halide-free, and generally selected as low cost, thermally and chemically stable, and easy to handle, such as titanium alkoxides [46–49].

In this context, this work aims to explore a new ALD process for the fabrication of Nb: TiO_2 films by combining titanium tetraisopropoxide (TTIP) and niobium(V) ethoxide (NEO) as precursor of Ti and Nb, respectively, and water as reactant. Moreover, the control of alternation of the metal oxides by ALD is the main parameter to vary the Nb doping concentration, leading to the variation of the optical and electrical properties. This parameter has been varied over a wide range in order to reach lower concentration than in previous works and investigating their impact on the films' properties. A low deposition temperature of 300 °C was selected targeting the anatase structure of the as-deposited (AD) films, unlike earlier works [10,45,48] at lower deposition temperature that produced amorphous films. Herein, the anatase structure of TiO_2 was targeted for the TCO application due to its wider band gap (3.2 eV), lighter electronic effective mass, higher electron mobility, and longer exciton lifetime compared to the ones of the rutile polymorph [50–52]. We sought to provide a detailed analysis of the effect of Nb dopant concentration and thermal annealing on the growth, crystal structure, microstructure, composition, and TCO properties of the fabricated films.

2. Materials and methods

The Nb: TiO_2 films were synthesized by thermal ALD technique using a Picosun® R-200 Advanced ALD equipment. The deposition chamber was maintained at a low pressure (4 hPa) by a vacuum pump. TTIP and NEO (Strem Chemicals Inc., 98% and 99% purity) kept at 75 and 180 °C were used as a precursor of Ti and Nb, respectively. Deionized water set at room temperature was used as a reactant. N_2 gas was used as carrier gas and for purging the reactor at 150 sccm flow rate. Deposition was performed using a common ALD temperature window for both precursors, where a substrate was maintained at 300 °C. A boron-doped p-type double-side polished Si (100) wafer substrate with 250±25 µm of thickness, 2 inches of diameter, and 5-15 Ω.cm of resistivity was used. Simultaneously, deposition on a glass substrate (SCHOTT D 263) was also carried out for optical studies.

The Nb: TiO_2 films were deposited by alternating cycles of TiO_2 layers with one cycle of niobium oxide (NbO_x), as illustrated in Figure 1, until reaching a total of 1000 cycles.

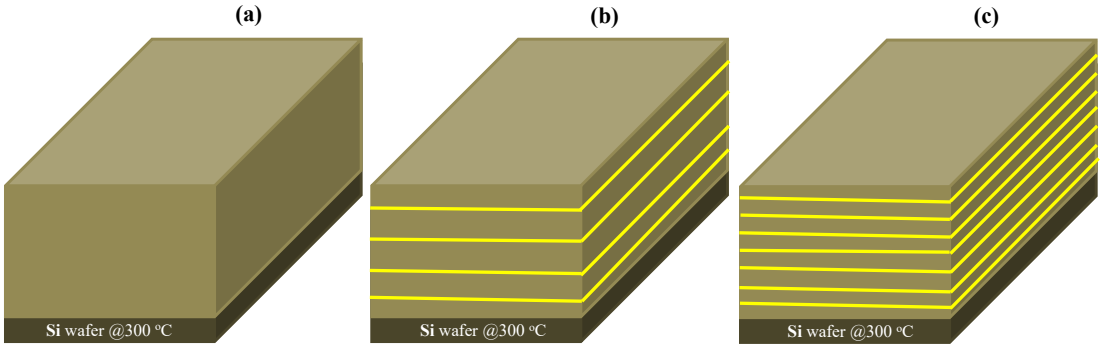

Figure 1: Schematic representation of ALD of the: (a) undoped TiO_2, (b and c) Nb:TiO_2 at various supercycles.

For TiO_2 deposition, the first half-cycle involved a 0.9 s pulse of TTIP, followed by a 4 s N2-purge of the reactor, the second-half cycle consists of a 3 s pulse of H_2O and a subsequent 4 s N_2-purge, as described in our previous work [48]. For NbO_x deposition, the first half-cycle consists a pulse of NEO during 2 s and 2 s of N_2-purging, and the second-half cycle involved a 2 s pulse of H_2O followed by a 2 s N_2-purge. The deposition conditions are summarized in Table 1. The Nb concentration was controlled by the dopant cycle ratio (R_{Nb}), which is defined as the ratio of the number of NbOx cycles (nNbOx) to the total number of TiO_2 and NbO_x cycles

(Equation 1). In this study, the R_{Nb} value ranges from 0 (undoped TiO_2 film) to 0.5 for the highest doped film.

$$R_{Nb} = \frac{\mathrm{nNbO_x}}{1000} \qquad \text{Equation (1)}$$

Table 1: Summary of the deposition conditions.

Targeted Film	**Nb: TiO_2**							
Deposited layers	TiO_2				NbO_x			
Half-cycles	1st half-cycle		2nd half-cycle		1st half-cycle		2nd half-cycle	
Precursor or reactant, and gas	TTIP	N_2	H_2O	N_2	NEO	N_2	H_2O	N_2
Bottle temperature, T_b (°C)	75		22		180		22	
Deposition temperature, T_d (°C)	300				300			
Pulse (s) / purge (s)	0.9 / 4		3 / 4		2 / 2		2 / 2	
Flow (sccm)	150		150		150		150	
Number of cycles	1000-$nNbO_x$				$nNbO_x$			
Total number of cycles	1000							
Thermal annealing, T_a (°C)	400, 500, 600							

Subsequently to deposition, the as-deposited (AD) films underwent thermal treatment through annealing at temperatures (T_a) of 400, 500, and 600 °C with a ramp rate of 1 °C/s for a duration of 1 hour under either N_2 or forming gas (N_2/H_2 95/5%).

The thickness and the complex refractive index ($n+ik$) of the films were determined using spectroscopic ellipsometry (SE) conducted with a Horiba Jobin-Yvon instrument. The I_s and I_c ellipsometric functions, which are derived from the Δ and ψ classical functions, were measured at an incidence angle of 70°, corresponding to the Brewster angle of Si [53]. The measurements were performed in the energy range between 1.5 and 6 eV, with a step of 0.05 eV. The measured data were fitted using the DeltaPsi2 software and a multilayer model structure (substrate/layer/rough layer/air). The substrate was characterized by reference dielectric functions, the layer employed Tauc-Lorentz (TL) functions, and the rough layer was

modeled using a Bruggeman effective medium combining the TL and air reference dielectric functions [54]. The growth per cycle (GPC) was determined by dividing the SE thickness of the film by the total number of ALD cycle.

The film's crystal structure was analyzed using grazing incidence X-ray diffraction (GI-XRD) with a D8 Advanced Brucker instrument. The instrument was equipped with a Cu Ka radiation source (λ=0.15418 nm), operated at 40 kV and 40 mA. X-ray reflectivity (XRR) measurements were conducted using a Bruker D8 Discover instrument to determine the electron density of the film. The structural properties were investigated through Raman spectroscopy using a *LabRAM HR EVOLUTION* Raman spectrometer (HORIBA Scientific). The spectrometer employed a laser emitting at 532 nm with a controlled power density of 0.52 MW cm^{-2} to prevent thermal effects. The measurements were performed at a spectral resolution of 0.8 cm^{-1} using 600 grooves/mm grating, an objective of 100x, and an acquisition time of 30 s. To minimize the effects of surface inhomogeneity and defocus, the reported data represent an average of three measurements taken at arbitrary positions on the film surfaces. Fourier-transform infrared (FTIR) spectra were collected using a Nicolet^{TM} iS50 FTIR instrument from Thermo Scientific. The measurement was conducted in far-infrared (FIR) regions, with 64 scans and a resolution of 8 cm^{-1}. The spectra were recorded at a 70° incidence angle, similar to the SE measurement, to activate transverse optical modes through the Berreman effect.

The microstructure of the films was pictured using High-Resolution Transmission Electron Microscopy (HRTEM). A double-corrected (probe and imaging) JEOL ARM 200F microscope equipped with a cold FEG (Field Emission Gun) source and operated at 200 kV was utilized. Chemical analyses were performed using an energy-dispersive X-ray (EDX) JEOL CENTURIO spectrometer and a high angle annular dark-field (HAADF) detector. This allowed for Z-contrast imaging (STEM HAADF) with a theoretical spatial resolution of 0.78 Å, as well as chemical mapping (STEM-EDX) at a nanometer scale. The thin foils for TEM analysis were prepared using a dual beam focused ion beam (FIB) setup (FEI Helios nanolab 660) with a FIB resolution of 2.54 nm at 30 kV. To protect the film surfaces during preparation, a thin

carbon layer (a few tens of nm) was deposited on the top of the film, followed by a platinum film (a few microns). All digitized images were processed using the commercial Digitalmicrograph® software from GATAN. In addition, Field Emission Gun Scanning Electron Microscopy (FEG-SEM) was also employed to observe the surface morphology and determine the grain size of the films.

The surface and in-depth chemical analysis, as well as the oxidation states of the metallic elements, were studied using X-ray photoelectron spectroscopy (XPS). A K-Alpha spectrometer from ThermoFisher Scientific equipped with a monochromatic Al-Kα X-ray source (*hv*=1486.6 eV) was used for the analysis. The beam diameter of 400 µm was used for surface points, while a smaller beam diameter of 200 µm was used for sputtered areas. Survey scans were collected in the full energy range (0-1100 eV) at a pass energy of 200 eV with a step size of 1 eV. High-resolution spectra were obtained at 40 eV with a step size of 0.2 eV. To acquire depth profiles, Ar+ ion sputtering was performed using a low mode of 500 eV and a raster width of 500 microns. Measurements were taken at different depths, but only spectra collected at the film surface are presented due to the strong impact of Ar+ ion sputtering on the oxidation states of all elements. It is important to note that carbon detected at the surface is attributed to air contamination and not present in the film. Therefore, the metallic ratio is based on an average of the Ti and Nb contents measured at all measurement depths of the films and not just at the surface.

The TCO properties of films were assessed through several measurements, including spectral transmittance, reflectance, and resistivity. To evaluate the optical properties, the optical transmittance and specular reflectance of the films deposited on a glass substrate were measured using a PerkinElmer 1050 Lambda UV-Vis-NIR spectrophotometer. The measurements were taken at an 8° incidence angle without polarization. Reflectance spectra were collected using the Universal Reflectance Accessory (URA). The electrical properties of the films were characterized by measuring their resistivity at room temperature. This was done using a 4-point probe technique in a square configuration with 1x1 mm^2 contacts positioned at

the corners. The measurement followed the van der Pauw method, and the current range used was between -20 and +20 nA.

3. Results and discussion

3.1. Structural and compositional properties

All the subsequent results presented below are for films deposited on Si (100) wafer substrates, otherwise, the substrate will be specified. The thickness for the AD films with R_{Nb}=0 and 0.1 over the entire Si wafer was estimated by SE using a 37 points map (Figure SI.1). The relative variation of the thickness over the entire 2-inch wafer was calculated using Equation SI.1, resulting in values of 10% and 3.84% for the undoped TiO_2 and the Nb: TiO_2 (R_{Nb}=0.1), respectively. This indicates a significant improvement in film thickness homogeneity due to Nb doping, compared to the undoped film. The enhanced thickness homogeneity can be attributed to the nature of the surface roughness and crystal structure. Smooth surfaces with high thickness homogeneity are characteristic of amorphous films, while rough surfaces with low thickness homogeneity usually occur in polycrystalline structures [55,56]. These aspects will be further discussed in the following sections: GI-XRD, Raman, and TEM results.

Figure 2a depicts the variation of the total thickness (layer + rough layer) as a function of R_{Nb} for the AD and the annealed films at various T_a. The AD TiO_2 film exhibits a thickness of 54 nm, corresponding to a growth per cycle (GPC) of 0.054 nm/cycle, which is comparable to a previous study that utilized $TiCl_4$ and water deposited at 300 °C [57]. It is worth noting that the GPC in our work is slightly higher than the range of 0.040 to 0.047 nm/cycle observed for films deposited between 200-250 °C using various precursors [44–46,58]. When TiO_2 is doped with Nb at R_{Nb}=0.005 and 0.01, the film thickness slightly increases to 58 nm, followed by a progressively drop as the R_{Nb} increases up to 0.1. Subsequently, the thickness slightly increased again as R_{Nb} increased from 0.1 to 0.5 (Figure 2a). The general trends of the thickness as a function of R_{Nb} remained consistent after annealing, although the values slightly

increased with higher annealing temperature (T_a). This effect was more pronounced for lower R_{Nb} values compared to higher ones (Figure 2a).

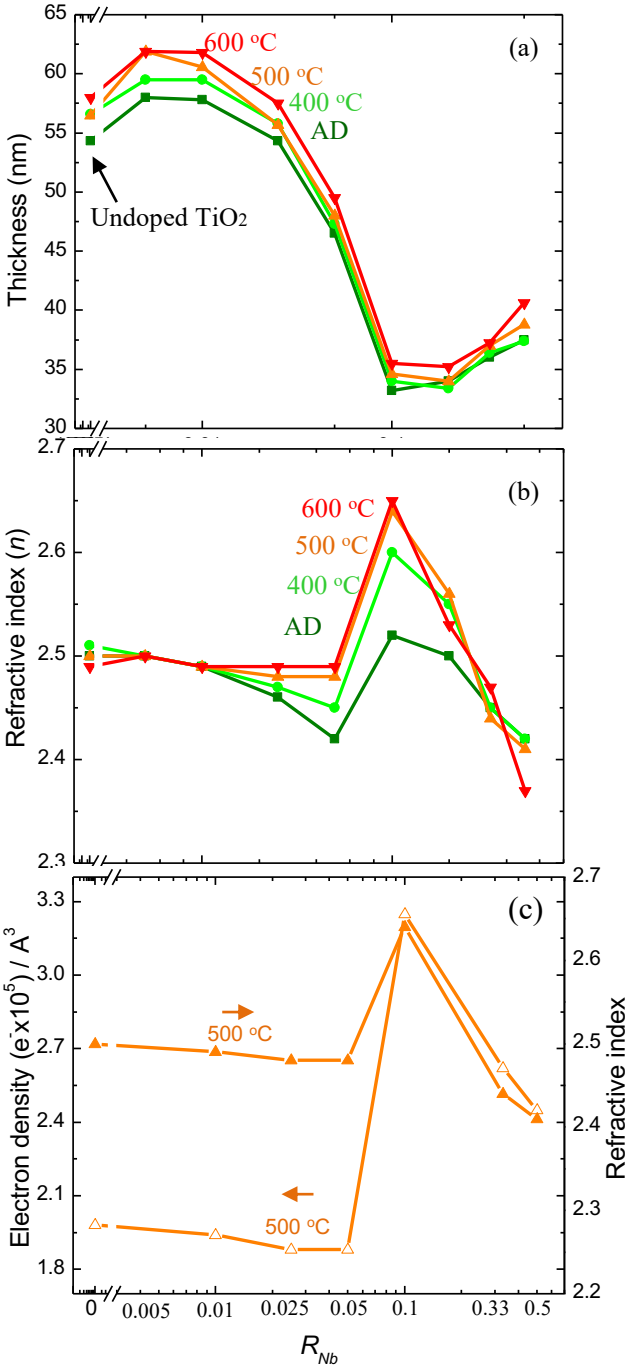

Figure 2: Variation of the: (a) total thickness, (b) refractive index, n (@1.95 eV), (c) electron density and refractive index, as a function of R_{Nb} for the AD and annealed films at various temperatures, Ta.

Figure 2b illustrates the changes in refractive index, *n* (at 1.95 eV) as a function of R_{Nb} for the AD and the annealed films. The AD undoped TiO_2 film exhibits an *n* value of 2.50,

corresponding to that of anatase TiO_2 [49]. As the dopant is introduced into TiO_2 structure up to R_{Nb}=0.05, the refractive index decreases to 2.40. This decrease in *n* suggests a progressive amorphization of the films caused by the incorporation of Nb, as the refractive index of amorphous TiO_2 is known to be lower than the one of anatase [59–61]. After annealing, the *n* at R_{Nb}=0.025 and 0.05 increase again to 2.50, indicating the crystallization of the amorphous material into anatase. At R_{Nb}=0.1, there is a drastic increase in *n* for both the as prepared and annealed films, followed by a decrease with the increases of R_{Nb} to 0.5 (Figure 2b). The variation of *n* and electron density (determined by XRR, SI) with R_{Nb} is plotted in Figure 2c, revealing a similar tendency. This supports the refractive index and the electronic population relationship in solid materials [62,63]. Furthermore, the drop in film thickness at R_{Nb}=0.1 (Figure 2a) can be attributed to the densification of the film [61].

Although the exact cause of the drastic rise of *n* and electron density at R_{Nb}=0.1 is not yet well understood and two hypotheses are considered: (i) a phase transformation into rutile, as the refractive index of rutile (2.8) is greater than that of anatase TiO2 (2.5) [64]; or (ii) an alteration on the growth orientation (without phase transformation), resulting higher density [65]. These two hypotheses will be further discussed in the subsequent sections that analyze the structural properties using the GI-XRD and Raman results.

Figure 3(a) depicts GI-XRD patterns normalized to the strong peak of the AD films as a function of R_{Nb}. Films with R_{Nb}=0-0.1 exhibits peaks at 25.3° and 48°, corresponding to the diffraction of (101) and (200) planes of anatase, respectively. For R_{Nb}=0.1, an additional anatase peak at 37.8° for (004) emerges. These peaks indicate that the AD films contain a certain proportion of crystalline anatase phase up to R_{Nb}=0.1. Beyond this R_{Nb}, the films are most likely amorphous or contain a low proportion of crystallites below the detection limit of the GI-XRD apparatus. However, due to the significantly decreased signal-to-noise ratio at R_{Nb}=0.1, it can be inferred that the proportion of anatase crystallites progressively decreases. Additionally, the FWHM (Figure 3c) of the (101) peak increases, suggesting a decrease in the size average of the crystallites and/or an increase in their internal stress. Furthermore, a progressive shift to

lower diffraction angles is observed as R_{Nb} increases from 0 to 0.1 (Figure 3c, and Figure SI.3a). This shift can be attributed to lattice expansion caused by the substitution of Ti with an ionic radius of 0.605 Å by Nb with a larger ionic radius of 0.64 Å [20,66,67].

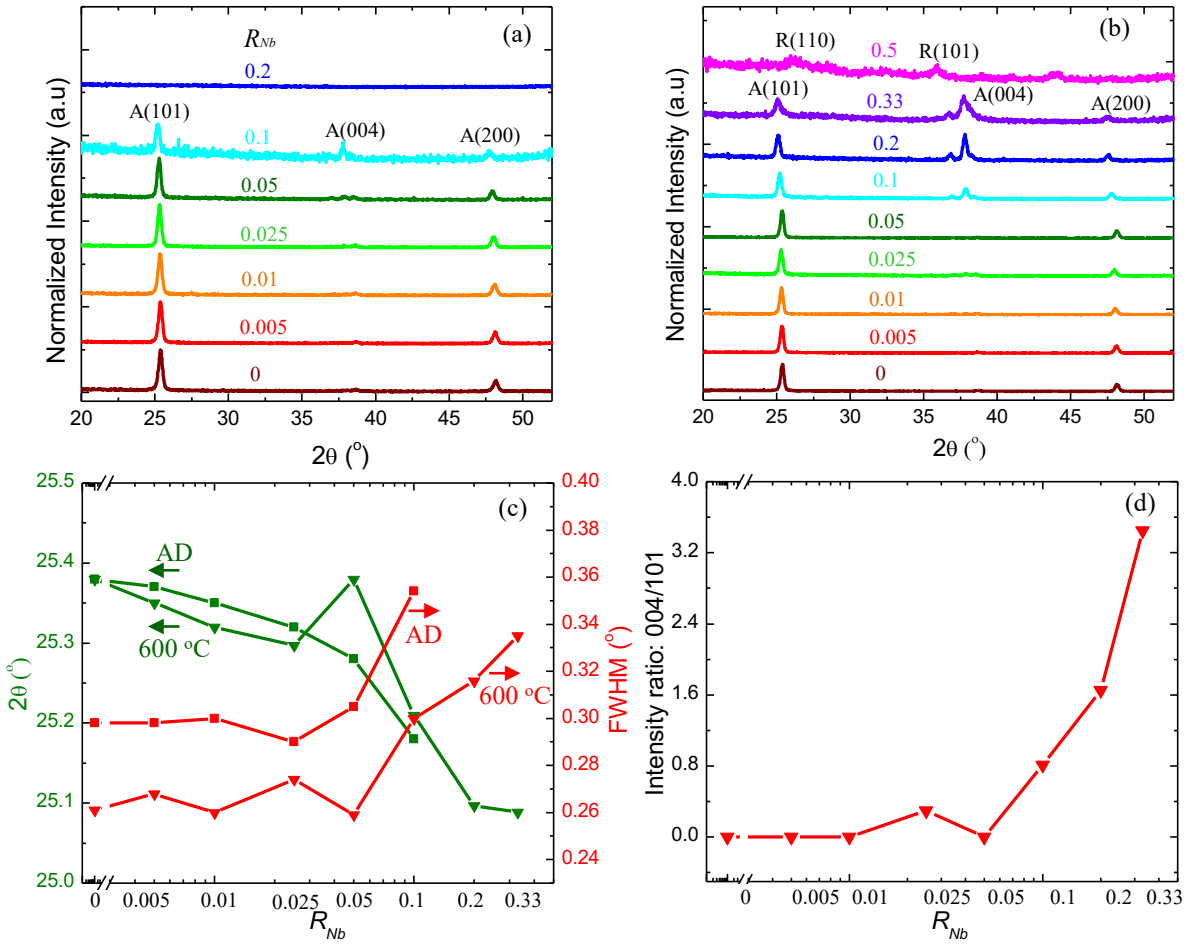

Figure 3: GI-XRD patterns of films: (a) AD, (b) T_a=600 °C. (c) peak positions (2θ) and FWHM of the (101) peak for AD and at T_a=600 °C, (d) peak intensity ratio of (004) over (101) at Ta=600 °C, as a function of R_{Nb}.

After annealing at T_a=600 °C the films continue to exhibit anatase patterns up to a higher R_{Nb}=0.33 (Figure 3b). At R_{Nb}=0.2 and 0.33, the annealed films show peaks of (101), (004), and (200) indicating that a certain proportion of the amorphous material has partially transformed into anatase. However, this proportion appears to decrease with increasing R_{Nb}, as evidenced by the decrease in the signal-to-noise ratio from R_{Nb}=0.1 to 0.33. The 2θ value of the (101) peak (Figure 3c, Figure SI.3b) also shows a similar shift to a lower diffraction angle as the R_{Nb}

increases from 0 to 0.33. However, the FWHM of the (101) peaks exhibit a significant reduction compared to the AD peaks (Figure 3c). This reduction can be explained by an increase in the size of the crystallites and/or the release of residual stress. Considering that annealing generally results in a stress relaxation and/or crystallite growth, the maintenance of the shift in the (101) peak diffraction, with increasing R_{Nb}, suggests its attribution to the substitution of Ti by Nb.

The intensity ratio of the (004) peak to the (101) peak is presented in Figure 3d as a function of R_{Nb}. For $R_{Nb} < 0.05$, the ratio is close to zero, indicating that growth orientation is primarily dominated by the (101) direction, as clearly demonstrated in Figure 3b. However, as the R_{Nb} increases from 0.05 to 0.1, the intensity ratio of (004) to (101) increases, and for R_{Nb}=0.2 and 0.33, the value is greater than 1 (Figure 3d). This indicates a change in the growth orientation starting from R_{Nb}=0.1, which could follow the (001) direction [41], in agreement with the increase in n (Figure 2b). The film at R_{Nb}=0.5 exhibits a different diffraction pattern with peaks at 26° and 36°, corresponding to (110) and (101) orientation, respectively, of rutile TiO_2 (Figure 3b). The intensity of the rutile peak is weak, indicating that the phase transformation to rutile at high Nb content is only partial. This can be attributed to the inherent tendency of Nb oxides to crystallize into rutile structure, as observed in previous studies [68].

However, no matter the R_{Nb} and T_a, no diffraction peaks corresponding to Nb oxides such as NbO, NbO_2, Nb_2O_5 were observed. It could be either explained by the fact that NbO_x is amorphous or its quantity is below the detection threshold limit. Furthermore, it implies the good incorporation of Nb into the TiO_2 lattice, most likely by substitution.

The structural properties of the films were further investigated using Raman spectroscopy. Figure 4a shows the Raman shift of the AD thin films and of the Si (100) wafer substrate (added for clarification) as a function of R_{Nb}. The undoped TiO_2 (R_{Nb}=0) shows four peaks attributed to anatase TiO_2 [52,69]. The Raman modes of E_g (~140 and 195 cm^{-1}) and B_{1g} (~393 cm^{-1}) are assigned to the O-Ti-O bending vibrations, while Eg (~636 cm^{-1}) is for Ti-O stretching vibrations [52,70]. Moreover, films deposited on glass substrate presents similar anatase

spectra with an additional peak at 516 cm^{-1} (Figure SI.4) assigned to the Ti-O stretching vibrations that is masked by the intense 520 cm^{-1} LO mode of the Si wafer (Figure 4a). No Raman peaks attributed to rutile or other phases of TiO_2 were detected in agreement with the GI-XRD results.

The above-mentioned Raman peaks are also seen in Nb: TiO_2 films up to R_{Nb}=0.1 indicating that the anatase structure is maintained, whereas no Raman peaks were observed in films produced with R_{Nb} >0.1 which is may explained by the fact that the latter films are mainly amorphous in agreement with the GI-XRD patterns. As R_{Nb} increases from 0 to 0.1, the principal peak of E_g (~140 cm^{-1}) mode shows a decrease in intensity, a blue shift (from 140 to 147 cm^{-1}), and a broadening (Figure 4a, inset). The decrease in peak intensity can be associated with the decreases in both the film thickness and the crystal/amorphous proportions [45]. Moreover, the substitution of Ti by Nb can form a new Nb-O-Ti bond that could distort the Ti-O-Ti bond. As a result, the Raman mode shows a broadening and a blue shift of the peaks [71]. These two observations increases as more of Nb replaces Ti [70].

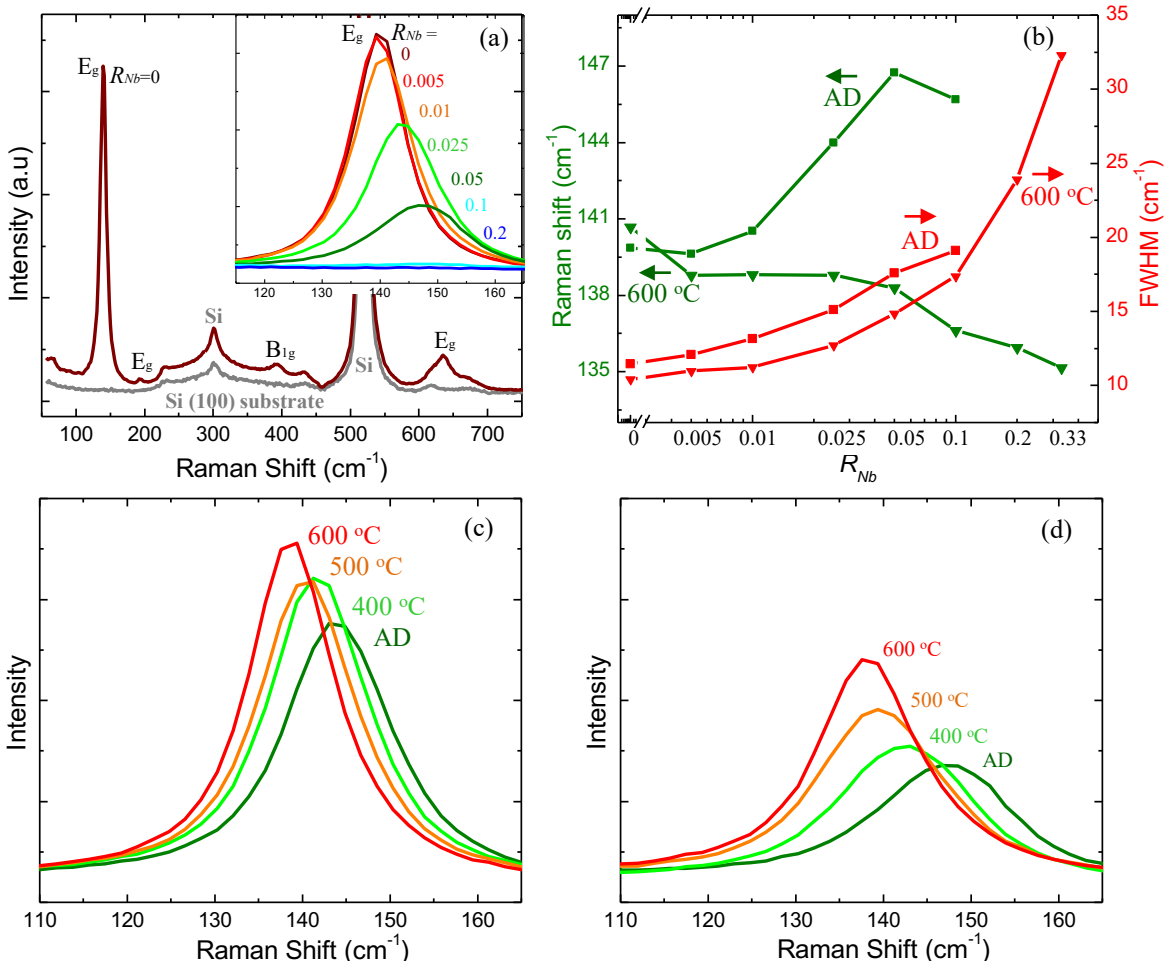

Figure 4: Raman spectra of: (a) the Si (100) substrate, and AD TiO_2. The E_g mode centered at 140-147 cm^{-1} for the undoped and doped films (AD) are shown as a function of R_{Nb} (a, inset). (b) Raman positions and FWHM of the E_g mode (centered ~140 cm^{-1}) determined using a Gaussian fit, as a function of R_{Nb} for the AD and T_a=600 °C. Raman spectra of E_g mode (centered ~140 cm^{-1}) for (c) R_{Nb}=0.025 , and (d) R_{Nb}=0.05 as a function of T_a.

The Raman spectra of the AD films before and after annealing confirms the important impact of the annealing process. Figures 4c and 4d show the evolution of the principal E_g modes of R_{Nb}=0.025 and 0.05 in the AD and at various T_a. When the T_a increases, the peak shifts towards the lower wavenumber, increases its intensity, and narrows its width in comparison with the AD film. This can be also seen in Figure 4b, displaying the variation of the peak positions (Raman shift) as a function of R_{Nb} for the AD and at T_a=600 °C. With increasing of R_{Nb}, the peak positions of the annealed films shifted to a lower wavenumber, which is in contrast to the AD that shows a shift to a higher wavenumber (Figure 4b). In addition, the FWHM values of

the annealed films are lower than the corresponding AD films. All these observations indicate that the crystal structure of films increases with annealing.

Figure 5(a) shows the far-FTIR spectra of the AD films at variable R_{Nb}. The undoped TiO_2 (R_{Nb}=0) spectra show two bands with maximum intensity centered at 260 and 434 cm^{-1}, and two shoulders at ~310 and ~410 cm^{-1} that are assigned to the TO_1, TO_3, TO_2, and TO_4, respectively, of anatase transverse optical modes [58,72,73]. The intensity of the TO_1 and TO_3 bands decreases with increasing the R_{Nb} from 0 to 0.05, which is explained by the progressive decrease of the anatase proportion up to the emergence of broad and weak bands starting from R_{Nb}=0.1. This latter FTIR signature is attributed to amorphous TiO_2 phase [57] with a structural organization that precedes anatase. The TO_1 and TO_3 bands show a shift to lower wavenumbers as the R_{Nb} increases due to the distortion of the anatase structure that may results from the Nb substitution, in agreement with the GI-XRD and Raman results.

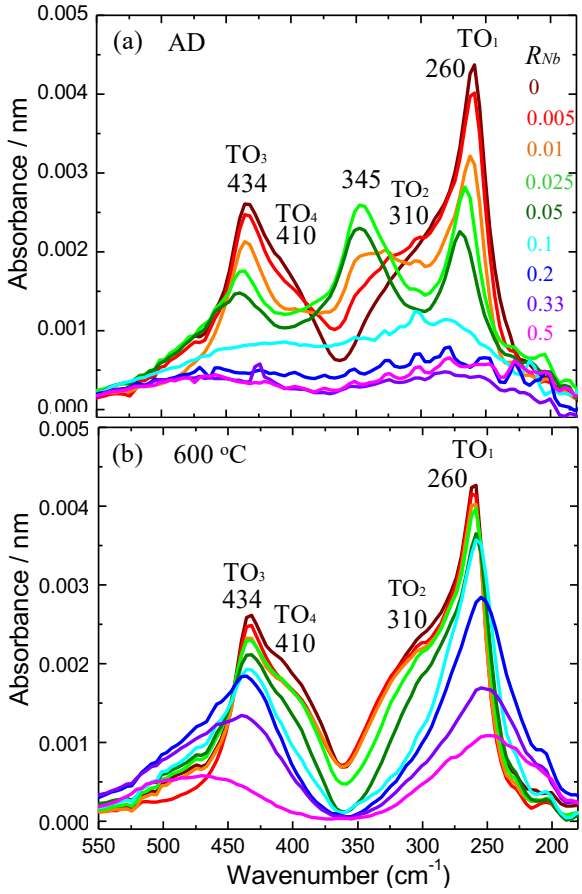

Figure 5: FTIR spectra of TiO_2 and Nb: TiO_2 thin films in far-infrared region: (a) AD, (b) Ta=600 °C, measured at an incidence angle of 70°. The intensity was normalized by the film thickness.

Interestingly, the AD Nb:TiO_2 films with R_{Nb} ranging from 0.005 to 0.05 exhibit a new vibrational band centered at ~345 cm^{-1} (Figure 5a). It is observed that the relative intensity of this band compared to the main TO_1 and TO_3 bands increase with increasing R_{Nb} from 0 to 0.025, followed by a slight decrease at R_{Nb}=0.05, and eventually, this band disappears in the amorphous films. To the best of our knowledge, such an intermediate band has not been reported for Nb:TiO_2. One can hypothesize that this band is either due to the formation of a new TOT bond (e.g. Ti-O-Nb), or/and is due to structural distortion of anatase caused by the incorporation of Nb. The anatase organization is clearly improved after annealing, as indicated by the increase of TO_4/TO_3 and TO_2/TO_1 intensity ratios at low R_{Nb} shows (Figure 5b), and the crystal proportion is enhanced at high R_{Nb} in full agreement with XRD and Raman spectra. This evolution at low R_{Nb} is concomitant with the loss of the 345 cm^{-1} peak, which may be also explained by the crystal organization improvement and/or by the segregation of Nb.

The microstructures of the films were investigated by TEM and SEM, and the dopant distribution was analyzed using STEM-EDX. Figure 6 shows a cross-sectional TEM images of the films (R_{Nb}=0, 0.025, and 0.1) at T_a=500 °C. At the film/Si-substrate interface, a thin layer of a few nanometers of native SiO_2 is seen. The film thicknesses estimated from the TEM images are in full agreement with the ones obtained by SE (Figure 2a). Nb doping brings significant effects on the surface roughness and the grain sizes. A rough surface is observed in the undoped TiO_2 (R_{Nb}=0) while the roughness decreases at R_{Nb}=0.025, and drops significantly at R_{Nb}=0.1 (Figure 6). This is also consistent with the roughness determined by SE (Figure SI.5), showing values ranging from 6 to 11 nm for $0<R_{Nb}<0.025$, and from 0.5 to 2 nm for $0.05<R_{Nb}<0.5$. Interestingly, the decrease in roughness occurs concomitantly with the increase of the film thickness surface homogeneity (Figure SI.1) as observed elsewhere [57]. Besides, the above-observed changing of structure from anatase to amorphous phase (XRD, Raman, and FTIR results) can explain the changing of surface from rough to smooth. Interestingly, the

grain size enlarged throughout the entire thickness with increasing of R_{Nb} compared to the undoped TiO_2 (Figure 6, and Figure SI.6). The estimated grain sizes are approximately in the ranges of 20-100, 70-200, and 300-800 nm for R_{Nb}=0, 0.025, and 0.1, respectively. This trend is in agreement with some previous studies [60]. We obtained smooth layers with very large nanocrystals compared to the thickness at high R_{Nb}, in the same manner as Pore, et al [41] through the crystallization of amorphous Nb:TiO_2 at 600 °C, as demonstrates the evolution of XRD, Raman, and FTIR results with annealing. In contrast, the roughness of already crystallized AD layers at low R_{Nb} remains almost unchanged and relatively (to the thickness) high after annealing.

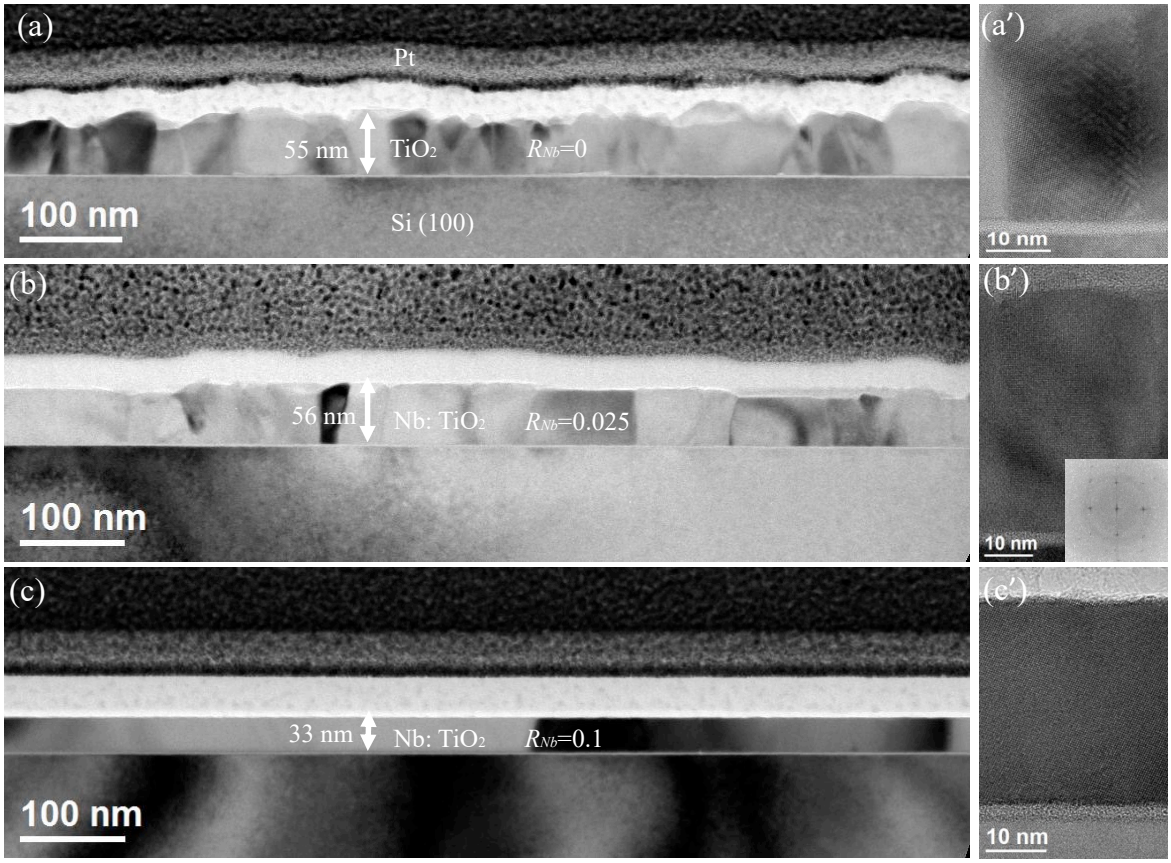

Figure 6: Cross sectional bright field TEM and their HRTEM images of films for R_{Nb}= (a, a') 0, (b, b') 0.025, and (c, c') 0.1, at Ta=500 °C.

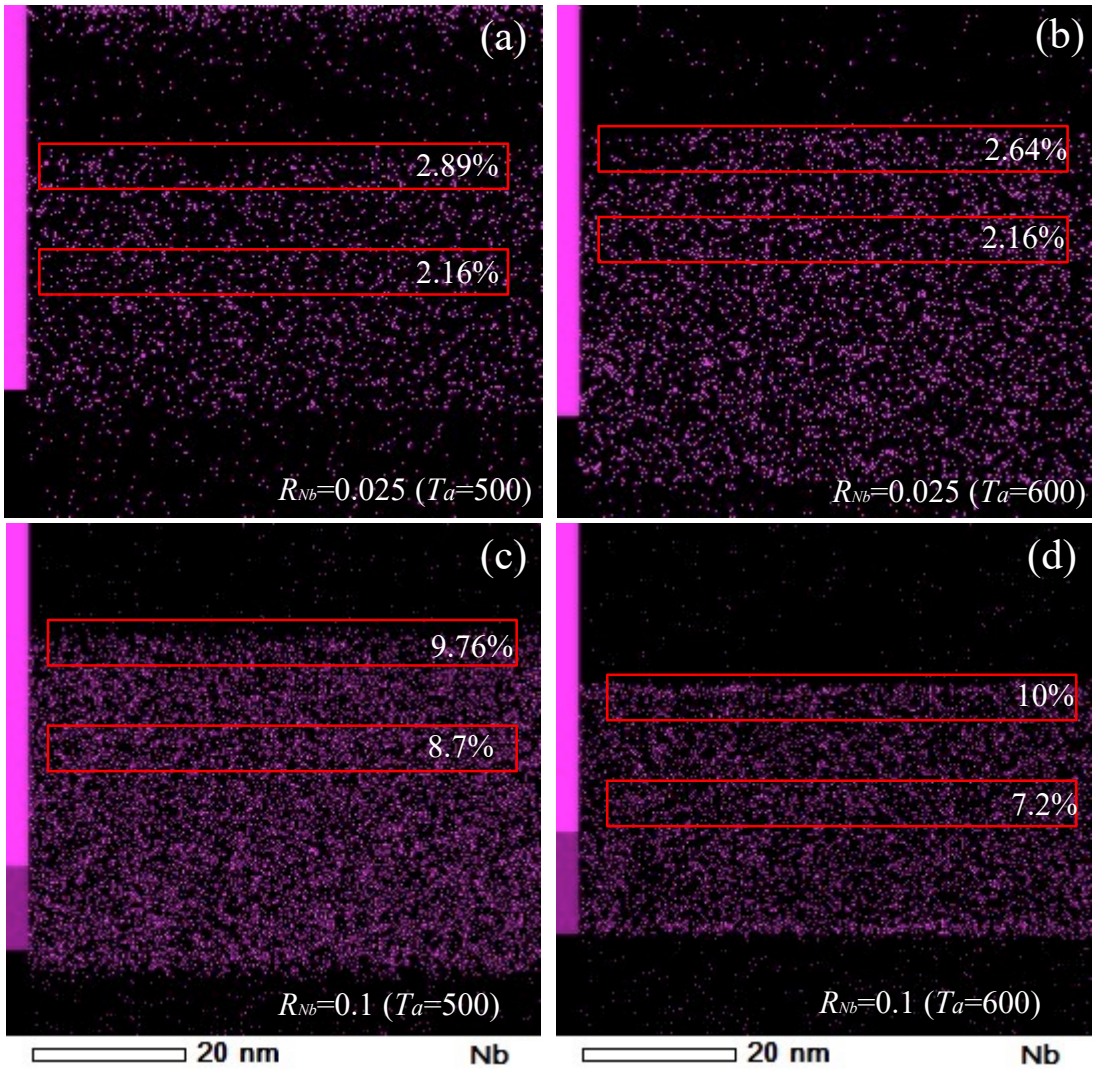

Figure 7: Elemental mapping of Nb in the films for R_{Nb}=0.025 and 0.1, at T_a=500 and 600 °C.

The elemental mapping, illlustrated in Figure 7, reveals that the distributions of the Nb dopant throughout the annealed film are not perfectly uniform, as there appears to be a segregation of the dopant at the top and bottom of the films, which increases with T_a. The EDX data indicates that the Nb concentration at the top of the film is higher compared to the interior of the film, suggesting that Nb diffused from the inner to the exterior of the film during annealing. Further information on the elements compositions is obtained from the XPS analysis of the samples. The XPS depth profiles are utilized to determine the dopant fraction (DF) by applying Equation 2.

$$DF = \frac{[Nb]}{[Nb]+[Ti]} \qquad \text{Equation (2)}$$

With, [Nb] and [Ti] are the atomic concentrations of Nb and Ti in the film, respectively, obtained by XPS and STEM-EDX.

The results are plotted on Figure 8 which illustrates the *DF* obtained by XPS and STEM-EDX as a function of R_{Nb}, showing good agreement of both techniques. It can be observed that the measured *DF* content is almost two times higher than the set R_{Nb} indicateing that the atomic NbO_x deposited layers hinder the deposition of TiO_2 in the ALD process. This partially explained by the decrease of the thickness by increasing the R_{Nb} (Figure 2a).

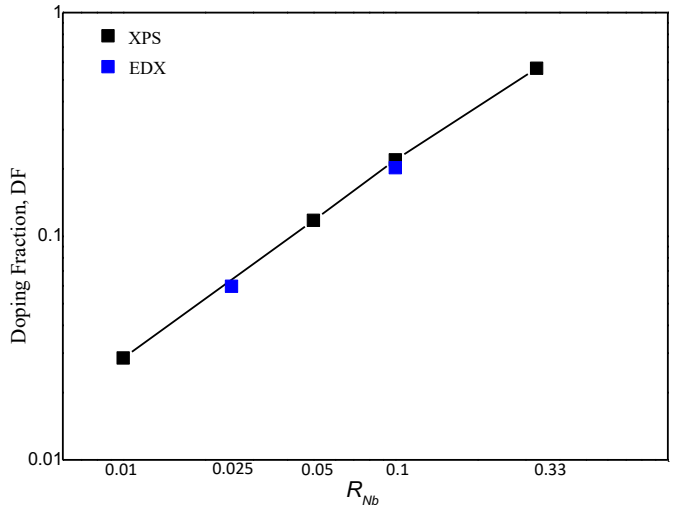

Figure 8: Nb metallic doping fraction (DF) determined by XPS and STEM-EDX versus the dopant cycle ratio (R_{Nb}) for films annealed at T_a=600 °C.

Figure 9(a-c) shows the normalized high-resolution XPS spectra of Ti 2p, Nb 3d, and O 1s for the annealed films at T_a=600 °C with varying R_{Nb} *value* (R_{Nb}=0.01, 0.05, 0.1, and 0.33), as well as their fit with various oxidation states contributions. The Ti 2p spectra (Figure 9a) exhibit doublet peaks with binding energy (BE) ranging from 458.6 to 459.0 eV (Ti $2p_{3/2}$) and from 464.5 to 464.9 eV (Ti $2p_{1/2}$), which are assigned to the oxidation state of Ti^{4+} (TiO_2) [19,28,74]. Additionally, a shoulder at 457.2 eV, assigned to Ti^{3+}, is observed and its intensity increases with R_{Nb} (Figure 9d). This could indicate the presence of either oxygen vacancies [75–78], resulting in the formation of Ti^{3+}, or, more likely, the donor nature of the Nb^{5+} dopant creating excess charges that are compensated by Ti^{3+} defects. These Ti^{3+} defects serve as efficient

donor states, leading to n-type conductivity [11]. Therefore, this observation further supports the substitution of Ti by Nb, forming to Ti^{3+}-O-Nb^{5+} bands in the anatase structure [19].

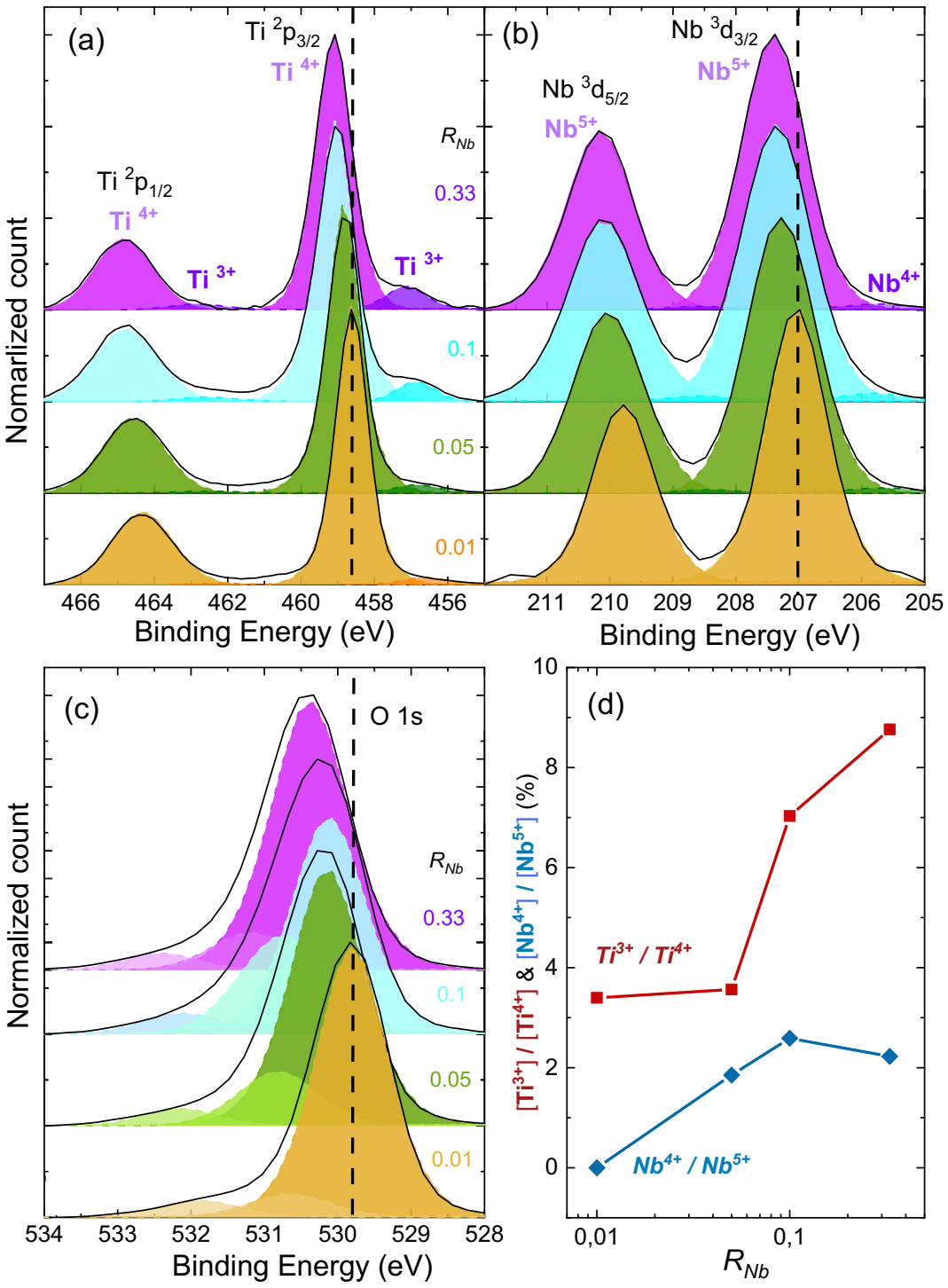

Figure 9: Normalized high-resolution XPS spectra at the surface for: (a) Ti 2p, (b) Nb 3d, and (c) O 1s (black lines), and their fit with several possible oxidation states components (full areas). (d) Percentage ratio of Ti^{3+}/Ti^{4+} and Nb^{4+}/Nb^{+5} concentration. These are for films annealed at T_a=600 °C.

In Figure 9b, the spectra exhibit two main peaks of Nb $3d_{5/2}$ (207.0-207.4 eV) and Nb $3d_{3/2}$ (209.8-210.1 eV) assigned to oxidation states of Nb^{5+} [79,80]. A weak contribution of Nb^{4+} progressively emerges at a binding energy (BE) of 205.8 eV with increasing of R_{Nb}. In addition to Ti^{3+}, the presence of Nb^{4+} introduce donor states, which can enhance the conductivity of the anatase-based n-type semiconductor. The O 1s XPS spectra (Figure 9c) consist of peaks at around 530 eV, assigned to Ti^{4+}-O bond, and a peak at approximately 531.5 eV, corresponding to O-H group [74]. As R_{Nb} increases, all XPS peaks undergo a progressive shift towards higher BE, which can be attributed to the lattice expansion caused by the larger electronegativity of Nb (1.6) compared to that of Ti (1.54) [74,81]. Interestingly, contrary to the findings of the aforementioned authors [74], we observe an increase in both Ti^{3+} and Nb^{4+} donor states. This could result in the elevation of the Fermi level energy [82] further into the conduction band, providing an explanation for the observed shift of the XPSs' peaks.

To further investigate this hypothesis, the optical and electrical properties were examined and discussed in the subsequent section.

3.2. TCO properties

The optical properties of the films were examined by measuring the transmittance (shown in Figure SI.7a) and the specular reflectance of the films deposited on a glass substrate and annealed at 500 °C under forming gas (N_2/H_2, 95/5%). The chosen annealing temperature was determined based on the thermal limit of the substrate. Since TCO materials find applications in a wide range of fields, it is important to assess their transmittance performance across a broad spectral range. To evaluate the transmittance efficiency, $E_{T(\lambda)}^{AM1.5}$, the integration of the solar irradiance AM1.5, $L_{AM1.5}$, was carried out as a reference standardized irradiance. The transmittance (T) of the films was measured within a common spectral range of 400-1000 nm, which encompasses the visible range as well as the PV conversion range. This range was chosen to estimate the transmittance efficiency using Equation 3 [83].

$$E_{T(\lambda)}^{AM1.5}(\%) = \frac{\int_{\lambda_{min}}^{\lambda_{max}} T(\lambda) * L_{AM1.5}(\lambda) d\lambda}{\int_{\lambda_{min}}^{\lambda_{max}} L_{AM1.5}(\lambda) d\lambda} \; x \; 100 \qquad \text{Equation 3}$$

Figure 10a displays the integrated transmission efficiency of the undoped TiO_2 and Nb:TiO_2 films, with values ranging from 66 to 81% as R_{Nb} increases from 0 to 0.5. Almost all the doped films exhibit better transmittance compared to the undoped films, except at R_{Nb}=0.005, where the magnitude steadily increases with the increase of R_{Nb}. This behavior can be attributed to the non-monotonic variation in film thickness within the range of 32-63 nm, despite the constant ALD number of cycles (1000) (as shown in Figure 2a). This thickness variation can lead to non-monotonic changes in transmittance between films [84,85]. However, Figure 10a demonstrates a consistent increase in $E_{T(\lambda)}^{AM1.5}$ with R_{Nb}, indicating a significant enhancement in film's transparency through Nb incorporation. Accordingly, the doped films at R_{Nb}=0.005 and 0.5 with thicknesses of 56 and 38 nm present transmission efficiency of 66% and 81%, respectively.

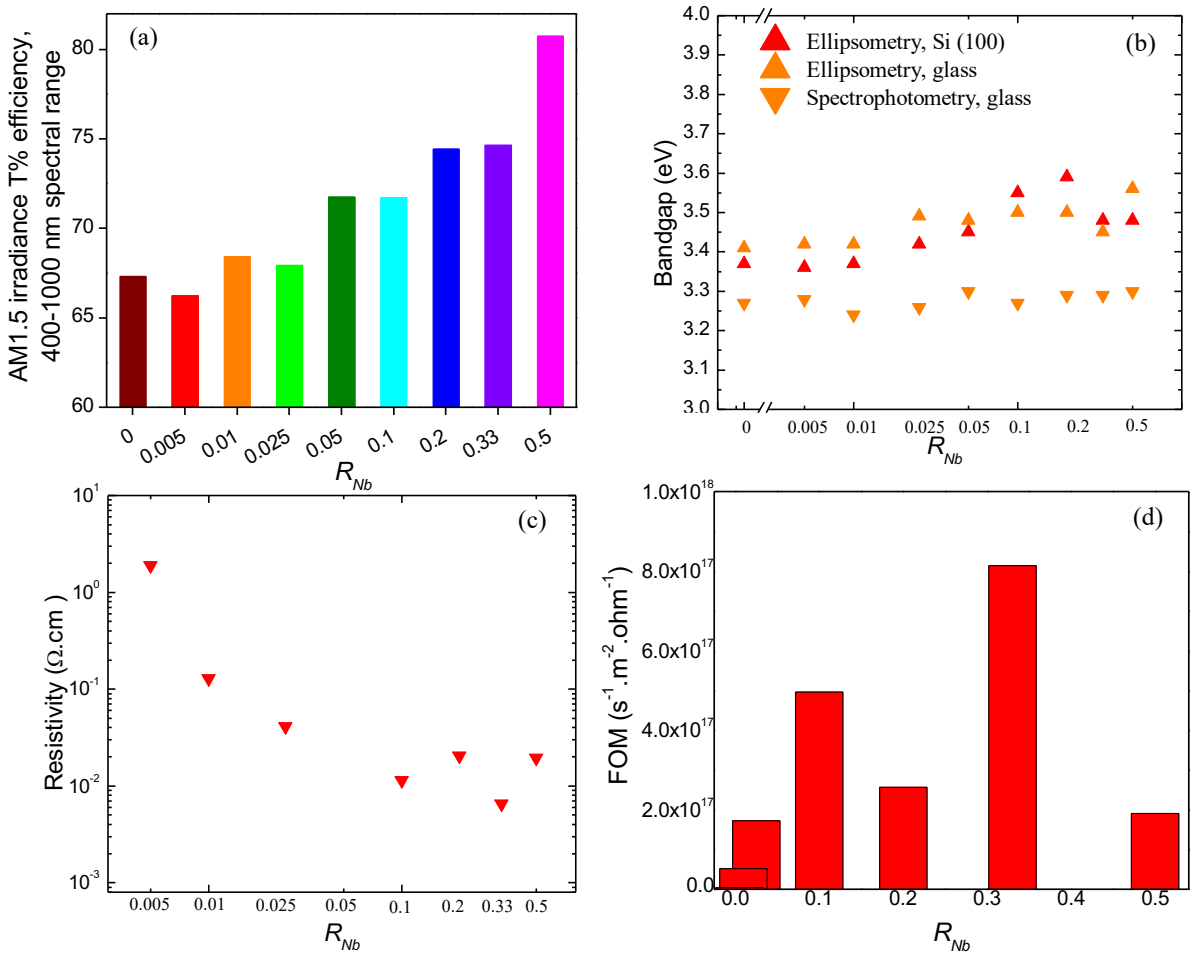

Figure 10: (a) Integrated transmission efficiency determined from the spectrophotometry data of films deposited on glass substrate, (b) optical bandgap energy estimated by spectroscopic ellipsometry and spectrophotometry for films deposited on Si (100) wafer and glass substrate, T_a=500 °C under forming gas: N_2/H_2, 95/5%. (c) Resistivity, and (d) Figure of merit of films with variable R_{Nb} annealed at T_a=600 °C under forming gas.

The optical bandgap energy (E_g) is determined using the transmittance and reflectance data and applying the Tauc plot (Equation 3) [86].

$$\alpha h\nu = B\left(h\nu - E_g\right)^n \qquad \text{Equation 3}$$

where, α is the absorption coefficient, $h\nu$ is the photon energy, B is the an energy independent constant, and n is a parameter that describe the type of optical transitions: n=2 for indirect transitions in anatase TiO_2 [87]. The absorption coefficient (α) can be determined using Equation 4.

$$\alpha(\lambda) = \frac{ln[1-R(\lambda)-T(\lambda)]}{d} \qquad \text{Equation 4}$$

where, R and T are the absolute reflectance and transmittance, respectively, and d is the thickness determined by SE for films deposited on a glass substrate. The E_g can be estimated from the extrapolation of the linear fit of $(\alpha h\nu)^{1/n}$ to zero, by plotting $(\alpha h\nu)^{1/n}$ vs $h\nu$ (Figure SI.7b).

Since the optical properties of films are strongly dependent on the type of substrate and techniques applied, the E_g was also estimated by SE for films deposited on Si (100) wafer and on glass substrate for films annealed at T_a=500 °C (Figure 10b). The E_g values on glass estimated from the transmission and reflection data present values ranging from 3.23 to 3.30 eV, which is close to that of anatase TiO_2, and no significant difference due to the variation of R_{Nb} is observed. However, the corresponding films determined by SE present a higher value ranging from 3.40 to 3.56 eV, which slightly increases with increasing of R_{Nb}. This trend is also observed for films on Si (100) substrate (Figure 10b). The widening of E_g could be explained by the Burstein-Moss effect [88], where the Fermi-level located above the bottom of the conduction band increases with increasing electron density. This indicate a degenerate

semiconductor where the optical absorption edge involves vertical transitions from the filled valence band to the lowest unfilled level in the conduction band [43,88,89].

The conductive nature of the films was evaluated by measuring the resistivity at room temperature using a 4-point probe method. The resistivity of the films in the AD state was too high to be measurable with our set-up, in contrast with the annealed (T_a=600 °C under forming gas) samples (Figure 10c). This indicates that the annealing is a crucial step since the conductivity of Nb:TiO_2 also depends on the oxygen stoichiometry in addition to the dopant content as well as the structural organization [20]. At R_{Nb}=0.005, a film with resistance of approximately 2 Ω.cm was obtained, while the resistivity gradually decreases to several orders of magnitude as the R_{Nb} increases to 0.5, and the lowest resistivity is 6.60×10^{-3} Ω.cm at R_{Nb}=0.33.

The decrease in resistivity with increasing the R_{Nb} can be attributed to various factors. One possible contribution is the increase in Ti^{3+} and Nb^{4+} donor states, as observed in the XPS results (Figure 9a) [21,90–94]. Additionally, the significant increase in grain sizes with increasing R_{Nb}, as observed in the TEM images (Figure 6), leads to a reduction in electron scattering at the grain boundaries, which can also contribute to lowering the resistivity [23,42].

In the context of TCO applications, it is necessary to optimize the optical and electrical coating parameters. Depending on the specific device, transparent electrodes need to meet certain minimum requirements for optical transmission and electrical conductivity. Ideally, both parameters should be maximized, but their interaction often makes it challenging to achieve both criteria simultaneously [95]. The most commonly used Figure of Merit (FoM) for comparing TCO performance is the Haacke figure of merit [96], which considers the average optical transmission around 500 nm (the peak of the solar spectrum). TCOs are employed in various applications related to solar light, such as solar cells or photo(electro)chemical cells, where they serve as front contacts or integral parts of the converting device. Consequently, TCOs must possess specific electrical and optical characteristics that enhance the transmission of sunlight onto the absorbent film. It is important to note that evaluating TCOs based on

narrowband transmission alone may not provide a representative measure of their overall ability to transmit photons. The visible transmission spectrum provides valuable information about photon flux density and flux-weighted solar photon transmission. By integrating T(%) over the entire solar spectrum, it becomes possible to evaluate the photocurrent density carried by a TCO when exposed to white light and assess this integral relative to the resistance sheet, Rsheet, of the film. This analysis helps identify the optimal balance between the transmission and resistance properties of the TCOs. Therefore, instead of relying solely on narrowband transmission, we propose utilizing the global air mass 1.5 photon flux spectrum (AM1.5g) to analyze the maximum photocurrent density (JPH) for a given TCO.

Therefore, we calculate the FoM (Figure 10d) as the ratio of JPH over R_{sheet} [97] for all our samples with increasing of Nb content, and compare with 20 nm thick commercial ITO film (CEC100) on glass sample provide by PGO-online company [98]. The results clearly demonstrate that the ITO layer outperforms all the samples tested in this study, with a FoM lower than $1.0x10^{18}$ s^{-1} m^{-2} Ω^{-1}. This highlights the fact that our material is not yet able to compete with commercial TCOs such as standard ITO. However, this FoM enables us to compare and analyze our samples more deeply. We achieve an eightfold improvement in the FoM for doped samples at R_{Nb}=0.33, which is the highest value among all the samples, compared to the undoped sample at R_{Nb}=0. For further Nb incorporation (R_{Nb}>0.33), the FoM decreases due to a decrease in transmittance on the AM1.5g spectral range.

4. Conclusion

Our newly developed ALD process utilizing TTIP and NEO precursors at a low substrate temperature of 300 °C has successfully synthesized Nb:TiO_2 thin films. The controlled dopant fraction, determined by R_{Nb}, has a significant impact on the growth rate as well as the structure, morphology, optical, and electrical properties of the films. We have observed that the actual dopant fraction obtained is nearly twice as high as the set point defined by R_{Nb}, which can be attributed to the inhibitory effect of Nb oxide layers on the growth of Ti oxide. Notably, as R_{Nb} increases, we have observed an improvement in the homogeneity of film thickness and an

increase in the size of anatase grains, accompanied by a decrease in surface roughness. This behavior is explained by the progressive amorphization of the as-deposited films with increasing R_{Nb}, as evidenced by various characterization techniques (GI-XRD, Raman, and FTIR), followed by the formation of larger and more uniform grains during annealing. Specifically, the AD films exhibit a crystalline anatase phase for R_{Nb}=0-0.1, while films with R_{Nb}>0.1 remain amorphous until inducing the crystallization by annealing. XRD, Raman, and FTIR results provide clear evidence of Ti substitution by Nb. Additionally, XPS spectra demonstrate an increase in the Ti and Nb content in the Ti^{3+} and Nb^{4+} oxidation states with increasing R_{Nb}. This increase in the donor states partially accounts for the observed decrease in resistivity. The introduction of Nb doping enhances the TCO properties of TiO_2, resulting in an increase in optical transmission efficiency of up to 15% and a decrease in resistivity of up to 10^{-3} Ω.cm. By employing, a FoM established over a wide spectral range using AM1.5g irradiance, a comparison of TCO performance reveals an eightfold improvement through Nb doping, with the highest FoM achieved for the film produced with an R_{Nb} of 0.33. This improvement on the performance paves the way for utilizing this material in solar radiation photoconversion applications. Furthermore, there are several potential ways for further improvement, such as optimizing the Nb doping process or exploring doping with other elements exhibiting interesting electronic configurations, such as vanadium (V) or Nb/V co-doping.

Acknowledgments

The authors are very grateful to the Normandy region (France) for the financial support through SUNRISE RIN-project.

Conflicts of Interest

The authors declare no conflict of interest

References

[1] O. Brian, G. Michael, A low-cost, high-efficiency solar cell based on dye-sensitized

colloidal TiO_2 films, Nature. 354 (1991) 737–740.

[2] D.S. Bhachu, S. Sathasivam, G. Sankar, D.O. Scanlon, G. Cibin, C.J. Carmalt, I.P. Parkin, G.W. Watson, S.M. Bawaked, A.Y. Obaid, S. Al-Thabaiti, S.N. Basahel, Solution processing route to multifunctional titania thin films: Highly conductive and photcatalytically active Nb:TiO_2, Adv. Funct. Mater. 24 (2014) 5075–5085. https://doi.org/10.1002/adfm.201400338.

[3] R.G. Gordon, Criteria for choosing transparent conductors, MRS Bull. 25 (2000) 52–57. https://doi.org/10.1557/mrs2000.151.

[4] J. Müller, B. Rech, J. Springer, M. Vanecek, TCO and light trapping in silicon thin film solar cells, Sol. Energy. 77 (2004) 917–930. https://doi.org/10.1016/j.solener.2004.03.015.

[5] A. Stadler, Transparent Conducting Oxides—An Up-To-Date Overview, Materials (Basel). 5 (2012) 661–683. https://doi.org/10.3390/ma5040661.

[6] R.A. Afre, N. Sharma, M. Sharon, M. Sharon, transparent conducting oxide films for various applications : a review, Rev. Adv.Mater.Sci. (2018) 79–89.

[7] Y. Ohhata, F. Shinoki, S. Yoshida, Optical properties of r.f. reactive sputtered tin-doped In2O3 films, Thin Solid Films. 59 (1979) 255–261. https://doi.org/10.1016/0040-6090(79)90298-0.

[8] T. Hitosugi, A. Ueda, Y. Furubayashi, Y. Hirose, S. Konuma, T. Shimada, T. Hasegawa, Fabrication of TiO_2-based transparent conducting oxide films on glass by pulsed laser deposition, Japanese J. Appl. Physics, Part 2 Lett. 46 (2007) 44–47. https://doi.org/10.1143/JJAP.46.L86.

[9] T. Hitosugi, A. Ueda, S. Nakao, N. Yamada, Y. Furubayashi, Y. Hirose, T. Shimada, T. Hasegawa, Fabrication of highly conductive Ti1-x Nbx O2 polycrystalline films on glass substrates via crystallization of amorphous phase grown by pulsed laser deposition,

Appl. Phys. Lett. 90 (2007) 1–4. https://doi.org/10.1063/1.2742310.

[10] G. Luka, L. Wachnicki, R. Jakiela, E. Lusakowska, Structural properties and metallic conductivity of Ti1-xNbxO2 films grown by atomic layer deposition on crystalline substrates, J. Phys. D. Appl. Phys. 48 (2015) 495305. https://doi.org/10.1088/0022-3727/48/49/495305.

[11] D. Casotti, V. Orsini, A. di Bona, S. Gardonio, M. Fanetti, M. Valant, S. Valeri, Ageing effects on electrical resistivity of Nb-doped TiO 2 thin films deposited at a high rate by reactive DC magnetron sputtering, Appl. Surf. Sci. 455 (2018) 267–275. https://doi.org/10.1016/j.apsusc.2018.05.068.

[12] A. Favier, D. Muñoz, S. Martín De Nicolás, P.J. Ribeyron, Boron-doped zinc oxide layers grown by metal-organic CVD for silicon heterojunction solar cells applications, Sol. Energy Mater. Sol. Cells. 95 (2011) 1057–1061. https://doi.org/10.1016/j.solmat.2010.11.013.

[13] J.S. Na, G. Scarel, G.N. Parsons, In situ analysis of dopant incorporation, activation, and film growth during thin film ZnO ZnO:Al Atomic layer deposition, J. Phys. Chem. C. 114 (2010) 383–388. https://doi.org/10.1021/jp908332q.

[14] K.T. Ramakrishna Reddy, T.B.S. Reddy, I. Forbes, R.W. Miles, Highly oriented and conducting ZnO:Ga layers grown by chemical spray pyrolysis, Surf. Coatings Technol. 151–152 (2002) 110–113. https://doi.org/10.1016/S0257-8972(01)01593-6.

[15] Y. Wu, A.D. Giddings, M.A. Verheijen, B. Macco, T.J. Prosa, D.J. Larson, F. Roozeboom, W.M.M. Kessels, Dopant Distribution in Atomic Layer Deposited ZnO:Al Films Visualized by Transmission Electron Microscopy and Atom Probe Tomography, Chem. Mater. 30 (2018) 1209–1217. https://doi.org/10.1021/acs.chemmater.7b03501.

[16] Y. Wu, P.M. Hermkens, B.W.H. Van De Loo, H.C.M. Knoops, S.E. Potts, M.A. Verheijen, F. Roozeboom, W.M.M. Kessels, Electrical transport and Al doping efficiency in

nanoscale ZnO films prepared by atomic layer deposition, J. Appl. Phys. 114 (2013). https://doi.org/10.1063/1.4813136.

[17] S.K. Kim, G.J. Choi, S.Y. Lee, M. Seo, S.W. Lee, J.H. Han, H.S. Ahn, S. Han, C.S. Hwang, Al-doped TiO_2 films with ultralow leakage currents for next generation DRAM capacitors, Adv. Mater. 20 (2008) 1429–1435. https://doi.org/10.1002/adma.200701085.

[18] J.H. Noh, H.S. Han, S. Lee, D.H. Kim, J.H. Park, S. Park, J.Y. Kim, H.S. Jung, K.S. Hong, A newly designed Nb-doped TiO_2/Al-doped ZnO transparent conducting oxide multilayer for electrochemical photoenergy conversion devices, J. Phys. Chem. C. 114 (2010) 13867–13871. https://doi.org/10.1021/jp104247t.

[19] T. Potlog, P. Dumitriu, M. Dobromir, A. Manole, D. Luca, Nb-doped TiO_2 thin films for photovoltaic applications, Mater. Des. 85 (2015) 558–563. https://doi.org/10.1016/j.matdes.2015.07.034.

[20] R.T. Tucker, N.A. Beckers, M.D. Fleischauer, M.J. Brett, Electron beam deposited Nb-doped TiO_2 toward nanostructured transparent conductive thin films, Thin Solid Films. 525 (2012) 28–34. https://doi.org/10.1016/j.tsf.2012.10.075.

[21] N. Yamada, T. Hitosugi, J. Kasai, N.L.H. Hoang, S. Nakao, Y. Hirose, T. Shimada, T. Hasegawa, Transparent conducting Nb-doped anatase TiO_2 (TNO) thin films sputtered from various oxide targets, Thin Solid Films. 518 (2010) 3101–3104. https://doi.org/10.1016/j.tsf.2009.07.205.

[22] C.H. Hsu, K. Te Chen, L.Y. Lin, W.Y. Wu, L.S. Liang, P. Gao, Y. Qiu, X.Y. Zhang, P.H. Huang, S.Y. Lien, W.Z. Zhu, Tantalum-doped TiO_2 prepared by atomic layer deposition and its application in perovskite solar cells, Nanomaterials. 11 (2021) 1–14. https://doi.org/10.3390/nano11061504.

[23] N.L.H. Hoang, N. Yamada, T. Hitosugi, J. Kasai, S. Nakao, T. Shimada, T. Hasegawa,

Low-temperature fabrication of transparent conducting anatase Nb-doped TiO_2 films by sputtering, Appl. Phys. Express. 1 (2008) 1150011–1150013. https://doi.org/10.1143/APEX.1.115001.

[24] T. Hitosugi, A. Ueda, S. Nakao, N. Yamada, Y. Furubayashi, Y. Hirose, S. Konuma, T. Shimada, T. Hasegawa, Transparent conducting properties of anatase Ti0.94Nb0.06O2 polycrystalline films on glass substrate, Thin Solid Films. 516 (2008) 5750–5753. https://doi.org/10.1016/j.tsf.2007.10.028.

[25] Y. Furubayashi, T. Hitosugi, Y. Yamamoto, K. Inaba, G. Kinoda, Y. Hirose, T. Shimada, T. Hasegawa, A transparent metal: Nb-doped anatase TiO_2, Appl. Phys. Lett. 86 (2005) 1–3. https://doi.org/10.1063/1.1949728.

[26] L. De Trizio, R. Buonsanti, A.M. Schimpf, A. Llordes, D.R. Gamelin, R. Simonutti, D.J. Milliron, Nb-doped colloidal TiO_2 nanocrystals with tunable infrared absorption, Chem. Mater. 25 (2013) 3383–3390. https://doi.org/10.1021/cm402396c.

[27] M. Fallah, M.R. Zamani-Meymian, M. Rabbani, Influence of two gradual steps of vacuum annealing on structural and opto-electronic characteristics of Nb-doped TiO_2 transparent conducting oxide, Superlattices Microstruct. 123 (2018) 242–250. https://doi.org/10.1016/j.spmi.2018.09.002.

[28] Y. Gao, S. Thevuthasan, D.E. McCready, M. Engelhard, MOCVD growth and structure of Nb- and V-doped TiO_2 films on sapphire, J. Cryst. Growth. 212 (2000) 178–190. https://doi.org/10.1016/S0022-0248(00)00010-5.

[29] X. Yang, Y. Min, S. Li, D. Wang, Z. Mei, J. Liang, F. Pan, Conductive Nb-doped TiO_2 thin films with whole visible absorption to degrade pollutants, Catal. Sci. Technol. 8 (2018) 1357–1365. https://doi.org/10.1039/c7cy02614e.

[30] J.R. Bakke, K.L. Pickrahn, T.P. Brennan, S.F. Bent, Nanoengineering and interfacial engineering of photovoltaics by atomic layer deposition, Nanoscale. 3 (2011) 3482–

3508. https://doi.org/10.1039/c1nr10349k.

[31] H. Kim, Atomic layer deposition of metal and nitride thin films: Current research efforts and applications for semiconductor device processing, J. Vac. Sci. Technol. B Microelectron. Nanom. Struct. 21 (2003) 2231. https://doi.org/10.1116/1.1622676.

[32] M. Leskelä, M. Ritala, Atomic layer deposition (ALD): From precursors to thin film structures, Thin Solid Films. 409 (2002) 138–146. https://doi.org/10.1016/S0040-6090(02)00117-7.

[33] V. Miikkulainen, M. Leskelä, M. Ritala, R.L. Puurunen, Crystallinity of inorganic films grown by atomic layer deposition: Overview and general trends, J. Appl. Phys. 113 (2013). https://doi.org/10.1063/1.4757907.

[34] R.L. Puurunen, Surface chemistry of atomic layer deposition: A case study for the trimethylaluminum/water process, J. Appl. Phys. 97 (2005). https://doi.org/10.1063/1.1940727.

[35] M. Knez, K. Nielsch, L. Niinistö, Synthesis and surface engineering of complex nanostructures by atomic layer deposition, Adv. Mater. 19 (2007) 3425–3438. https://doi.org/10.1002/adma.200700079.

[36] M. Leskelä, M. Ritala, Atomic Layer Deposition Chemistry: Recent Developments and Future Challenges, Angew. Chemie - Int. Ed. 42 (2003) 5548–5554. https://doi.org/10.1002/anie.200301652.

[37] V. Cremers, R.L. Puurunen, J. Dendooven, Conformality in atomic layer deposition: Current status overview of analysis and modelling, Appl. Phys. Rev. 6 (2019). https://doi.org/10.1063/1.5060967.

[38] S.M. George, Atomic layer deposition: An overview, Chem. Rev. 110 (2010) 111–131. https://doi.org/10.1021/cr900056b.

[39] R.W. Johnson, A. Hultqvist, S.F. Bent, A brief review of atomic layer deposition: From

fundamentals to applications, Mater. Today. 17 (2014) 236–246. https://doi.org/10.1016/j.mattod.2014.04.026.

[40] N.E. Richey, C. De Paula, S.F. Bent, Understanding chemical and physical mechanisms in atomic layer deposition, J. Chem. Phys. 152 (2020). https://doi.org/10.1063/1.5133390.

[41] V. Pore, M. Ritala, M. Leskelä, T. Saukkonen, M. Järn, Explosive crystallization in atomic layer deposited mixed titanium oxides, Cryst. Growth Des. 9 (2009) 2974–2978. https://doi.org/10.1021/cg801337f.

[42] J.P. Niemelä, Y. Hirose, K. Shigematsu, M. Sano, T. Hasegawa, M. Karppinen, Suppressed grain-boundary scattering in atomic layer deposited Nb:TiO_2 thin films, Appl. Phys. Lett. 107 (2015). https://doi.org/10.1063/1.4935425.

[43] J.P. Niemelä, Y. Hirose, T. Hasegawa, M. Karppinen, Transition in electron scattering mechanism in atomic layer deposited Nb:TiO_2 thin films, Appl. Phys. Lett. 106 (2015) 19–23. https://doi.org/10.1063/1.4906865.

[44] J.P. Niemelä, H. Yamauchi, M. Karppinen, Conducting Nb-doped TiO_2 thin films fabricated with an atomic layer deposition technique, Thin Solid Films. 551 (2014) 19–22. https://doi.org/10.1016/j.tsf.2013.11.043.

[45] W.J.H. (Willem-J. Berghuis, J. Melskens, B. Macco, S.B. Basuvalingam, M.A. Verheijen, W.M.M. (Erwin) Kessels, Atomic layer deposition of Nb-doped TiO_2 : Dopant incorporation and effect of annealing, J. Vac. Sci. Technol. A. 38 (2020) 022408-1–9. https://doi.org/10.1116/1.5134743.

[46] M. Ritala, M. Leskelä, L. Niinistö, P. Haussalo, Titanium Isopropoxide as a Precursor in Atomic Layer Epitaxy of Titanium Dioxide Thin Films, Chem. Mater. 5 (1993) 1174–1181. https://doi.org/10.1021/cm00032a023.

[47] J. Aarik, A. Aidla, T. Uustare, M. Ritala, M. Leskelä, Titanium isopropoxide as a

precursor for atomic layer deposition: Characterization of titanium dioxide growth process, Appl. Surf. Sci. 161 (2000) 385–395. https://doi.org/10.1016/S0169-4332(00)00274-9.

[48] A. Jolivet, C. Labbé, C. Frilay, O. Debieu, P. Marie, B. Horcholle, F. Lemarié, X. Portier, C. Grygiel, S. Duprey, W. Jadwisienczak, D. Ingram, M. Upadhyay, A. David, A. Fouchet, U. Lüders, J. Cardin, Structural, optical, and electrical properties of TiO_2 thin films deposited by ALD: Impact of the substrate, the deposited thickness and the deposition temperature, Appl. Surf. Sci. 608 (2023). https://doi.org/10.1016/j.apsusc.2022.155214.

[49] V. Pore, A. Rahtu, M. Leskelä, M. Ritala, T. Sajavaara, J. Keinonen, Atomic layer deposition of photocatalytic TiO_2 thin films from titanium tetramethoxide and water, Chem. Vap. Depos. 10 (2004) 143–148. https://doi.org/10.1002/cvde.200306289.

[50] T. Hitosugi, S.N. Naoomi Yamada, Y. Hirose, T. Hasegawa, Properties of TiO_2-based transparent conducting oxides.pdf, Phys. Status Solidi A. 7 (2010) 1529–1537.

[51] H. Tang, H. Berger, P.E. Schmid, F. Lévy, G. Burri, Photoluminescence in TiO_2 anatase single crystals, Solid State Commun. 87 (1993) 847–850. https://doi.org/10.1016/0038-1098(93)90427-O.

[52] H. Tang, K. Prasad, R. Sanjinès, P.E. Schmid, F. Lévy, Electrical and optical properties of TiO_2 anatase thin films, J. Appl. Phys. 75 (1994) 2042–2047. https://doi.org/10.1063/1.356306.

[53] https://www.horiba.com/cze/scientific/technologies/spectroscopic-ellipsometry/measurement-techniques/

[54] B. Horcholle, C. Labbé, X. Portier, P. Marie, C. Frilay, W. Yuan, W. Jadwisienczak, D. Ingram, C. Grygiel, J. Cardin, Growth and study of Tb3+ doped Nb2O5 thin films by radiofrequency magnetron sputtering: Photoluminescence properties, Appl. Surf. Sci.

597 (2022). https://doi.org/10.1016/j.apsusc.2022.153711.

[55] K. Kukli, M. Ritala, M. Leskelä, R. Lappalainen, Niobium Oxide Thin Films Grown by Atomic Layer Epitaxy, Chem. Vap. Depos. 4 (1998) 29–34. https://doi.org/10.1002/(sici)1521-3862(199801)04:01<29::aid-cvde29>3.3.co;2-i.

[56] R.L. Puurunen, T. Sajavaara, E. Santala, V. Miikkulainen, T. Saukkonen, M. Laitinen, M. Leskelä, Controlling the crystallinity and roughness of atomic layer deposited titanium dioxide films, J. Nanosci. Nanotechnol. 11 (2011) 8101–8107. https://doi.org/10.1166/jnn.2011.5060.

[57] D.R.G. Mitchell, G. Triani, D.J. Attard, K.S. Finnie, P.J. Evans, C.J. Barbé, J.R. Bartlett, Atomic layer deposition of TiO_2 and Al_2O_3 thin films and nanolaminates, Smart Mater. Struct. 15 (2006). https://doi.org/10.1088/0964-1726/15/1/010.

[58] A. Henegar, T. Gougousi, Stability and Surface Reactivity of Anatase TiO_2 Films.pdf, ECS J. Solid State Sci. Thechnology. (2015) 298–304.

[59] A. Bendavid, P.J. Martin, Review of thin film materials deposition by the filtered cathodic vacuum arc process at CSIRO, J. Aust. Ceram. Soc. 50 (2014) 86–101.

[60] A. V. Manole, M. Dobromir, M. Gîrtan, R. Mallet, G. Rusu, D. Luca, Optical properties of Nb-doped TiO_2 thin films prepared by sol-gel method, Ceram. Int. 39 (2013) 4771–4776. https://doi.org/10.1016/j.ceramint.2012.11.066.

[61] S. Ratzsch, E.B. Kley, A. Tünnermann, A. Szeghalmi, Influence of the oxygen plasma parameters on the atomic layer deposition of titanium dioxide, Nanotechnology. 26 (2015). https://doi.org/10.1088/0957-4484/26/2/024003.

[62] C.R. Ottermann, K. Bange, Correlation between the density of TiO_2 films and their properties, Thin Solid Films. 286 (1996) 32–34. https://doi.org/10.1016/S0040-6090(96)08848-7.

[63] K. Sangwal, W. Kucharczyk, Relationship between density and refractive index of

inorganic solids, J. Phys. D. Appl. Phys. 20 (1987) 522–525. https://doi.org/10.1088/0022-3727/20/4/019.

[64] A. Bendavid, P.J. Martin, H. Takikawa, Deposition and modification of titanium dioxide thin films by filtered arc deposition, Thin Solid Films. 360 (2000) 241–249. https://doi.org/10.1016/S0040-6090(99)00937-2.

[65] A. Bendavid, P.J. Martin, Å. Jamting, H. Takikawa, Structural and optical properties of titanium oxide thin films deposited by filtered arc deposition, Thin Solid Films. 355 (1999) 6–11. https://doi.org/10.1016/S0040-6090(99)00436-8.

[66] B.Y.R.D. Shannon, M. H, N.H. Baur, O.H. Gibbs, M. Eu, V. Cu, Revised Effective Ionic Radii and Systematic Studies of Interatomie Distances in Halides and Chaleogenides, Acta Cryst. (1976) 751–767.

[67] A.K. Chandiran, F. Sauvage, M. Casas-Cabanas, P. Comte, S.M. Zakeeruddin, M. Graetzel, Doping a TiO_2 photoanode with Nb^{5+} to enhance transparency and charge collection efficiency in dye-sensitized solar cells, J. Phys. Chem. C. 114 (2010) 15849–15856. https://doi.org/10.1021/jp106058c.

[68] D.Y. Lee, J.H. Park, Y.H. Kim, M.H. Lee, N.I. Cho, Effect of Nb doping on morphology, crystal structure, optical band gap energy of TiO_2 thin films, Curr. Appl. Phys. 14 (2014) 421–427. https://doi.org/10.1016/j.cap.2013.12.025.

[69] S. Sahoo, A.K. Arora, V. Sridharan, Raman line shapes of optical phonons of different symmetries in anatase TiO_2 nanocrystals, J. Phys. Chem. C. 113 (2009) 16927–16933. https://doi.org/10.1021/jp9046193.

[70] S. Seeger, K. Ellmer, M. Weise, D. Gogova, D. Abou-Ras, R. Mientus, Reactive magnetron sputtering of Nb-doped TiO_2 films: Relationships between structure, composition and electrical properties, Thin Solid Films. 605 (2016) 44–52. https://doi.org/10.1016/j.tsf.2015.11.058.

[71] B. Choudhury, M. Dey, A. Choudhury, Defect generation, d-d transition, and band gap reduction in Cu-doped TiO_2 nanoparticles, Int. Nano Lett. 3 (2013). https://doi.org/10.1186/2228-5326-3-25.

[72] A. Miquelot, O. Debieu, V. Rouessac, C. Villeneuve, N. Prud'homme, J. Cure, V. Constantoudis, G. Papavieros, S. Roualdes, C. Vahlas, TiO_2 nanotree films for the production of green H2 by solar water splitting: From microstructural and optical characteristics to the photocatalytic properties, Appl. Surf. Sci. 494 (2019) 1127–1137. https://doi.org/10.1016/j.apsusc.2019.07.191.

[73] R. Gonzalez, R. Zallen, H. Berger, Infrared reflectivity and lattice fundamentals in anatases, Phys. Rev. B - Condens. Matter Mater. Phys. 55 (1997) 7014–7017. https://doi.org/10.1103/PhysRevB.55.7014.

[74] H. Su, Y.T. Huang, Y.H. Chang, P. Zhai, N.Y. Hau, P.C.H. Cheung, W.T. Yeh, T.C. Wei, S.P. Feng, The Synthesis of Nb-doped TiO_2 Nanoparticles for Improved-Performance Dye Sensitized Solar Cells, Electrochim. Acta. 182 (2015) 230–237. https://doi.org/10.1016/j.electacta.2015.09.072.

[75] A. Aronne, M. Fantauzzi, C. Imparato, D. Atzei, L. De Stefano, G. D'Errico, F. Sannino, I. Rea, D. Pirozzi, B. Elsener, P. Pernice, A. Rossi, Electronic properties of TiO_2-based materials characterized by high Ti3+ self-doping and low recombination rate of electron-hole pairs, RSC Adv. 7 (2017) 2373–2381. https://doi.org/10.1039/c6ra27111a.

[76] K. Batalović, N. Bundaleski, J. Radaković, N. Abazović, M. Mitrić, R.A. Silva, M. Savić, J. Belošević-Čavor, Z. Rakočević, C.M. Rangel, Modification of N-doped TiO_2 photocatalysts using noble metals (Pt, Pd) - A combined XPS and DFT study, Phys. Chem. Chem. Phys. 19 (2017) 7062–7071. https://doi.org/10.1039/c7cp00188f.

[77] Y. He, O. Dulub, H. Cheng, A. Selloni, U. Diebold, Evidence for the predominance of subsurface defects on reduced anatase TiO_2(101), Phys. Rev. Lett. 102 (2009) 1–4. https://doi.org/10.1103/PhysRevLett.102.106105.

[78] D. Rafieian, W. Ogieglo, T. Savenije, R.G.H. Lammertink, Controlled formation of anatase and rutile TiO_2 thin films by reactive magnetron sputtering, AIP Adv. 5 (2015). https://doi.org/10.1063/1.4931925.

[79] T. Blanquart, K. Kukli, J. Niinistö, V. Longo, M. Heikkilä, M. Ritala, M. Leskelä, Optical and dielectric characterization of atomic layer deposited Nb 2O5 thin films, ECS Solid State Lett. 1 (2012) 3–6. https://doi.org/10.1149/2.002201ssl.

[80] S. Ouendi, C. Arico, F. Blanchard, J.L. Codron, X. Wallart, P.L. Taberna, P. Roussel, L. Clavier, P. Simon, C. Lethien, Synthesis of T-Nb2O5 thin-films deposited by Atomic Layer Deposition for miniaturized electrochemical energy storage devices, Energy Storage Mater. 16 (2019) 581–588. https://doi.org/10.1016/j.ensm.2018.08.022.

[81] N. Oka, Y. Sanno, J. Jia, S.I. Nakamura, Y. Shigesato, Transparent conductive Nb-doped TiO 2 films deposited by reactive dc sputtering using Ti-Nb alloy target, precisely controlled in the transition region using impedance feedback system, Appl. Surf. Sci. 301 (2014) 551–556. https://doi.org/10.1016/j.apsusc.2014.02.126.

[82] M. García-Tecedor, G. Gorni, F. Oropeza, L. Gómez, M. Liras, V.A. de la Peña O'Shea, M. Barawi, Unravelling nanostructured Nb-doped TiO_2 dual band behaviour in smart windows by in situ spectroscopies, J. Mater. Chem. A. 10 (2022) 19994–20004. https://doi.org/10.1039/d2ta03239b.

[83] A. Boileau, S. Hurand, F. Baudouin, U. Lüders, M. Dallocchio, B. Bérini, A. Cheikh, A. David, F. Paumier, T. Girardeau, P. Marie, C. Labbé, J. Cardin, D. Aureau, M. Frégnaux, M. Guilloux-Viry, W. Prellier, Y. Dumont, V. Demange, A. Fouchet, Highly Transparent and Conductive Indium-Free Vanadates Crystallized at Reduced Temperature on Glass Using a 2D Transparent Nanosheet Seed Layer, Adv. Funct. Mater. 32 (2022) 1–9. https://doi.org/10.1002/adfm.202108047.

[84] C. Jiang, Z. Wu, S. Xiao, Z. Ma, L. Liu, R.K.Y. Fu, P.K. Chu, H. Lin, F. Pan, Structural and optoelectrical properties of Nb-TiO_2 films fabricated by low-energy magnetron

sputtering and post-annealing, Surf. Coatings Technol. 365 (2019) 10–14. https://doi.org/10.1016/j.surfcoat.2018.05.092.

[85] Z.L. Tseng, L.C. Chen, J.F. Tang, M.F. Shih, S.Y. Chu, Thickness Effect of Nb-Doped TiO_2 Transparent Conductive Oxide Grown on Glass Substrates Fabricated by RF Sputtering, J. Electron. Mater. 46 (2017) 1476–1480. https://doi.org/10.1007/s11664-016-5180-3.

[86] J. Tauc, R. Grigorovici, A. Vancu, Optical Properties and Electronic Structure of Amorphous Germanium, Phys. Status Solidi. 15 (1966) 627–637. https://doi.org/10.1002/pssb.19660150224.

[87] N. Serpone, D. Lawless, R. Khairutdinov, Size effects on the photophysical properties of colloidal anatase TiO_2 particles: Size quantization or direct transitions in this indirect semiconductor?, J. Phys. Chem. 99 (1995) 16646–16654. https://doi.org/10.1021/j100045a026.

[88] E. Burstein, Anomalous optical absorption limit in InSb [4], Phys. Rev. 93 (1954) 632–633. https://doi.org/10.1103/PhysRev.93.632.

[89] I. Ben Jemaa, F. Chaabouni, L. Presmanes, Y. Thimont, M. Abaab, A. Barnabe, P. Tailhades, Structural, optical and electrical investigations on Nb doped TiO_2 radio-frequency sputtered thin films from a powder target, J. Mater. Sci. Mater. Electron. 27 (2016) 13242–13248. https://doi.org/10.1007/s10854-016-5471-8.

[90] N. Yamada, T. Hitosugi, J. Kasai, N.L.H. Hoang, S. Nakao, Y. Hirose, T. Shimada, T. Hasegawa, Direct growth of transparent conducting Nb-doped anatase TiO_2 polycrystalline films on glass, J. Appl. Phys. 105 (2009). https://doi.org/10.1063/1.3148267.

[91] Z. Yuan, J. Gong, S. Xu, Z. Li, G. Tang, Investigation of the thermoelectric properties of reduced Nb-doped TiO_2-δ ceramics, J. Alloys Compd. 710 (2017) 778–783.

https://doi.org/10.1016/j.jallcom.2017.03.336.

[92] R.K. Sharma, M.C. Bhatnagar, G.L. Sharma, Effect of Nb metal ion in TiO_2 oxygen gas sensor, Appl. Surf. Sci. 92 (1996) 647–650.

[93] K. Safeen, V. Micheli, R. Bartali, G. Gottardi, A. Safeen, H. Ullah, N. Laidani, Synthesis of conductive and transparent Nb-doped TiO_2 films: Role of the target material and sputtering gas composition, Mater. Sci. Semicond. Process. 66 (2017) 74–80. https://doi.org/10.1016/j.mssp.2017.04.012.

[94] D. Dorow-Gerspach, D. Mergel, M. Wuttig, Effects of different amounts of nb doping on electrical, optical and structural properties in sputtered TiO_2−x films, Crystals. 11 (2021) 1–13. https://doi.org/10.3390/cryst11030301.

[95] A.L. Dawar, J.C. Joshi, Semiconducting transparent thin films: their properties and applications, J. Mater. Sci. 19 (1984) 1–23. https://doi.org/10.1007/bf00552989.

[96] G. Haacke, New figure of merit for transparent conductors, Journal of Applied Physics 47, 4086–4089 (1976), https://doi.org/10.1063/1.323240

[97] J.A. Mendez-Gamboa, R. Castro-Rodriguez, I. V. Perez-Quintana, R.A. Medina-Esquivel, A. Martel-Arbelo, A figure of merit to evaluate transparent conductor oxides for solar cells using photonic flux density, Thin Solid Films. 599 (2016) 14–18. https://doi.org/10.1016/j.tsf.2015.12.038.

[98] PGO-online company, www.pgo.com